J|A|C|S
ARTICLES
Published on Web 12/13/2002

Spectroscopic and Electronic Structure Studies of the Diamagnetic Side-On Cu^{II}-Superoxo Complex $Cu(O_2)[HB(3\text{-}R\text{-}5\text{-}^{i}Prpz)_3]$: Antiferromagnetic Coupling versus Covalent Delocalization

Peng Chen,[†] David E. Root,[†] Cecelia Campochiaro,[†] Kiyoshi Fujisawa,*[,‡] and Edward I. Solomon*[,†]

Contribution from the Department of Chemistry, Stanford University, Stanford, California 94305, and Department of Chemistry, University of Tsukuba, Tsukuba 305-8571, Japan

Received July 16, 2002; E-mail: Edward.Solomon@stanford.edu; kiyoshif@chem.tsukuba.ac.jp

Abstract: Magnetic, vibrational, and optical techniques are combined with density functional calculations to elucidate the electronic structure of the diamagnetic mononuclear side-on Cu^{II}-superoxo complex. The electronic nature of its lowest singlet/triplet states and the ground-state diamagnetism are explored. The triplet state is found to involve the interaction between the Cu *xy* and the superoxide π_v^* orbitals, which are orthogonal to each other. The singlet ground state involves the interaction between the Cu *xy* and the in-plane superoxide π_σ^* orbitals, which have a large overlap and thus strong bonding. The ground-state singlet/triplet states are therefore fundamentally different in orbital origin and not appropriately described by an exchange model. The ground-state singlet is highly delocalized with no spin polarization.

1. Introduction

Oxygen activation by copper proteins is a very important process in biology.[1,2] Reactive Cu-oxygen intermediates play a central role in many biological enzymatic pathways and homogeneous catalytic cycles.[3−7] Mononuclear Cu^{II}-superoxo species are likely involved in the chemistry at several Cu protein active sites, such as Cu/Zn superoxide dismutase,[8] dopamine β-monooxygenase,[2] peptidylglycine α-hydroxylating monooxygenase,[9,10] and copper amine oxidase.[11] In synthetic copper/oxygen model chemistry, the mononuclear Cu^{II}-superoxo species is believed to be the precursor to oxygen binding and activation in peroxo/oxo bridged binuclear Cu complexes.[5,6,12,13] A number of mononuclear Cu^{II}-superoxo complexes have been synthesized and are EPR silent, indicating a diamagnetic ground state.[14−21] The diamagnetic property of the Cu^{II}-superoxo complex has been generally ascribed to the antiferromagnetic coupling between the spins on the Cu^{II} atom and the superoxide radical.[14,19]

The only structurally characterized Cu^{II}-superoxo complex, $Cu(O_2)[HB(3\text{-}^{t}Bu\text{-}5\text{-}^{i}Prpz)_3]$ (referred to as $L3CuO_2$, $HB(3\text{-}^{t}Bu\text{-}5\text{-}^{i}Prpz)_3$ = hydrotris(3-*tert*-butyl-5-isopropyl-1-pyrazolyl)borate), has the superoxide ligand bound in a side-on mode (Figure 1).[18,21] The complex has an O−O bond length of ∼1.22 Å and an O−O vibrational frequency of 1112 cm^{-1} in its IR spectrum, which shifts to 1060 cm^{-1} in the 18-oxygen isotope labeled sample, consistent with its description as a superoxide complex.[22] The +2 oxidation state of the Cu atom in the Cu^{II}-

[†] Stanford University.
[‡] University of Tsukuba.

(1) Solomon, E. I.; Sundaram, U. M.; Machonkin, T. E. *Chem. Rev.* **1996**, *96*, 2563.
(2) Klinman, J. P. *Chem. Rev.* **1996**, *96*, 2541.
(3) Solomon, E. I.; Chen, P.; Metz, M.; Lee, S.-K.; Palmer, A. E. *Angew. Chem., Int. Ed.* **2001**, *40*, 4570.
(4) Kitajima, N.; Moro-oka, Y. *Chem. Rev.* **1994**, *94*, 737.
(5) Que, L., Jr.; Tolman, W. B. *Angew. Chem., Int. Ed.* **2002**, *41*, 1114.
(6) Mahadevan, V.; Gebbink, R. J. M. K.; Stack, T. D. P. *Curr. Opin. Chem. Biol.* **2000**, *4*, 228.
(7) Liang, H. C.; Dahan, M.; Karlin, K. D. *Curr. Opin. Chem. Biol.* **1999**, *3*, 168.
(8) Strothkamp, K. G.; Lippard, S. J. *Acc. Chem. Res.* **1982**, *15*, 318.
(9) Prigge, S. T.; Mains, R. E.; Eipper, B. A.; Amzel, L. M. *Cell. Mol. Life Sci.* **2000**, *57*, 1236.
(10) Jaron, S.; Blackburn, N. J. *Biochemistry* **1999**, *38*, 15086.
(11) Dooley, D. M.; McGuirl, M. A.; Brown, D. E.; Turowski, P. N.; McIntire, W. S.; Knowles, P. F. *Nature* **1991**, *349*, 262.
(12) Blackman, A. G.; Tolman, W. B. In *Metal-Oxo and Metal-Peroxo Species in Catalytic Oxidations*; Meunier, B., Ed.; Springer-Verlag: Berlin, 2000; p 179.
(13) Kopf, M.-A.; Karlin, K. D. In *Biomimetic Oxidations Catalyzed by Transition Metal Complexes*; Meunier, B., Ed.; Imperial College Press: London, 2000; p 309.
(14) Nappa, M.; Valentine, J. S.; Miksztal, A. R.; Schugar, H. J.; Isied, S. S. *J. Am. Chem. Soc.* **1979**, *101*, 7744.
(15) Karlin, K. D.; Wei, N.; Jung, B.; Kaderli, S.; Zuberbuhler, A. D. *J. Am. Chem. Soc.* **1991**, *113*, 5868.
(16) Karlin, K. D.; Wei, N.; Jung, B.; Kaderli, S.; Niklaus, P.; Zuberbuhler, A. D. *J. Am. Chem. Soc.* **1993**, *115*, 9506.
(17) Wei, N.; Murthy, N. N.; Chen, Q.; Zubieta, J.; Karlin, K. D. *Inorg. Chem.* **1994**, *33*, 1953.
(18) Fujisawa, K.; Tanaka, M.; Moro-oka, Y.; Kitajima, N. *J. Am. Chem. Soc.* **1994**, *116*, 12079.
(19) Chaudhuri, P.; Hess, M.; Weyhermuller, T.; Wieghardt, K. *Angew. Chem., Int. Ed.* **1999**, *38*, 1095.
(20) Spencer, D. J. E.; Aboelella, N. W.; Reynolds, A. M.; Holland, P. L.; Tolman, W. B. *J. Am. Chem. Soc.* **2002**, *124*, 2108.
(21) There was a misassigned mononuclear end-on Cu^{II}-superoxo complex which was later reassigned as a mononuclear Cu^{II}-hydroxo complex. See: Berreau, L. M.; Mahapatra, Halfen, J. A.; Young, V. G.; Tolman, W. B. *Inorg. Chem.* **1996**, *35*, 6339. Harata, M.; Jitsukawa, K.; Masuda, H.; Einaga, H. *J. Am. Chem. Soc.* **1994**, *116*, 10817. Harata, M.; Jitsukawa, K.; Masuda, H.; Einaga, H. *Bull. Chem. Soc. Jpn.* **1998**, *71*, 637.
(22) Nakamoto, K. *Infrared and Raman Spectra of Inorganic and Coordination Compounds; Part A: Theory and Applications in Inorganic Chemistry*, 5th ed.; John Wiley & Sons: New York, 1997.

 10.1021/ja020969i CCC: $25.00

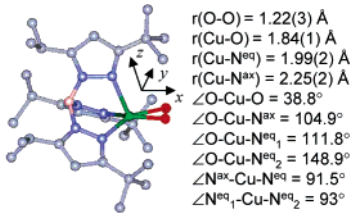

Figure 1. Crystal structure of Cu(O_2)[HB(3-^{t}Bu-5-^{i}Prpz)$_3$]. The CuO_2 plane is defined as *xy* with the *x*-axis bisecting the O−Cu−O angle.

superoxo complex is confirmed by its Cu K-edge X-ray absorption spectrum, which shows a small preedge feature at ~8979 eV, characteristic of a Cu^{II} center.[23,24]

In this study, we combine magnetic and spectroscopic characterizations with density functional calculations to elucidate the electronic structure of this side-on Cu^{II}-superoxo complex. The natures of the lowest singlet and triplet states of the complex were investigated, and a detailed description of the ground-state diamagnetism is developed to obtain insight into the magnetic properties and bonding interactions between Cu^{II} and the superoxide ligand. Over the course of this study, it was determined that there is some contamination of a dimeric L3Cu^{II}(O_2)Cu^{II}L3 component in solutions of the L3CuO_2 complex. As this dimer component has intense spectral features associated with the μ-η^2:η^2-O_2^{2-}-Cu$^{II}_2$ structure,[25] which obscure the Cu^{II}-superoxo spectral features, an analogous Cu(O_2)[HB(3-Ad-5-^{i}Prpz)$_3$] complex (referred to as L10CuO_2, HB(3-Ad-5-^{i}Prpz)$_3$ = hydrotris(3-adamantyl-5-isopropyl-1-pyrazolyl)borate) was synthesized. The adamantyl side chain on the pyrazole ring is much bulkier, preventing dimerization in the solution. The results obtained with the L10 ligand were combined with those of the L3 complex and used to determine the electronic structure of the side-on Cu^{II}-superoxo species.

2. Experimental Section

Materials and Synthesis. All reagents were of the highest grade commercially available and were used without further purification unless otherwise noted. Dichloromethane, diethyl ether, and toluene were carefully purified by distillation under argon atmosphere from P_2O_5 and sodium/bezophenone ketyl, respectively. Preparation and handling of air-sensitive materials were performed under an argon atmosphere using standard Schlenk techniques or a glovebox.

L3Cu^I(DMF). L3CuCl (0.45 g, 0.75 mmol)[26] was dissolved in 40 mL of CH_2Cl_2 and 10 mL of DMF. After the mixture was cooled at −50 °C, an excess amount of KO_2 solid was added to this solution. The color of this solution turned gradually to pale yellow from brownish red. After the reduction reaction was completed, the remaining KO_2 was removed by filtration with Celite. The filtrate was evaporated to dryness. The resultant solid was recrystallized from DMF at −30 °C to afford a colorless powder. Yield 0.27 g (56%). Anal. Calcd for $C_{33}H_{59}N_7BCuO$: C, 61.52; H, 9.23; N, 15.22. Found: C, 61.10; H, 9.11; N, 15.38. FTIR (cm^{-1}, KBr): ν(BH) 2530, ν(CO) 1661. ^{1}H NMR (δ/ppm, DCON(CD_3)$_2$, 400 MHz, 25 °C): 1.22 (d, J = 6.7 Hz, 18H, CH*Me*$_2$), 1.35 (s, 27H, C*Me*$_3$), 2.78 (s, 3H, HCON*Me*$_2$), 2.95 (s, 3H, HCON*Me*$_2$), 3.58 (m, J = 6.7 Hz, 3H, C*H*Me$_2$), 5.84 (s, 3H, pz-*H*), 8.02 (s, 1H, *H*CONMe$_2$).

L3CuO_2. L3Cu(DMF) (0.30 g) was dissolved in 10 mL of CH_2Cl_2. After this solution was cooled at −78 °C, dioxygen was introduced to this tube. After being recrystallized at −78 °C overnight, the reddish brown powder was collected by filtration. Anal. Calcd for $C_{30}H_{52}N_6BCuO_2$: C, 59.74; H, 8.69; N, 13.93; Found: C, 59.39; H, 8.85; N, 13.39. UV−vis (C_7H_8, 23 °C): 352 nm (ϵ, 2330 M^{-1} cm^{-1}), 510 nm (sh, 230), 660 nm (90). FTIR (cm^{-1}, KBr): ν(BH) 2564, ν(O−O) 1112 (ν(^{18}O−^{18}O) 1062), ν(Cu−O) 550 (ν(Cu−^{18}O) 532). Resonance Raman (cm^{-1}, CH_2Cl_2, 77 K, 363.8 nm ext): 308 ν(Cu_2O_2), 2ν(Cu−O) 1097 (2ν(Cu−^{18}O) 1050). (406.7 nm ext): ν(Cu−O) 554 (ν(Cu−^{18}O) 534). ^{1}H NMR (δ/ppm, CD_2Cl_2, 400 MHz, −40 °C): 1.19 (d, J = 6.4 Hz, 18H, CH*Me*$_2$), 1.66 (s, 27H, C*Me*$_3$), 3.36 (m, J = 6.4 Hz, 3H, C*H*Me$_2$), 6.19 (s, 3H, pz-*H*).

L10Cu^I(DMF). L10CuCl (0.40 g, 0.75 mmol)[26] was dissolved in 50 mL of CH_2Cl_2 and 10 mL of DMF. After being cooled at −50 °C, an excess amount of KO_2 solid was added to this solution. The color of this solution turned gradually to pale yellow from brownish red. After the reduction reaction was completed, the remaining KO_2 was removed by filtration with Celite. The filtrate was evaporated to dryness. The resultant solid was recrystallized from ether/CH_2Cl_2 at −30 °C to afford a colorless powder. Yield 0.26 g (58%). Anal. Calcd for **L10Cu(DMF)**·CH_2Cl_2, $C_{52}H_{79}N_7BCuOCl_2$: C, 64.82; H, 8.26; N, 10.18. Found: C, 64.78; H, 8.17; N, 9.67. FTIR (cm^{-1}, KBr): ν(BH) 2540, ν(CO) 1660. ^{1}H NMR (δ/ppm, CD_2Cl_2, 500 MHz, 20 °C): 1.22 (d, J = 6.9 Hz, 18H, CH*Me*$_2$), 1.79 (m, 18H, Ad-*H*δ), 2.06 (br, 9H, Ad-*H*β), 2.09 (br, 18H, Ad-*H*α), 2.82 (s, 3H, HCON*Me*$_2$), 2.91 (s, 3H, HCON*Me*$_2$), 3.44 (septet, J = 6.9 Hz, 3H, C*H*Me$_2$), 5.82 (s, 3H, pz-*H*), 7.96 (s, 1H, *H*CONMe$_2$).

L10CuO_2. L10Cu(DMF) (0.10 g) was dissolved in 5 mL of CH_2Cl_2. After this solution was cooled at −78 °C, dioxygen was introduced to this tube. After being recrystallized at −78 °C overnight, the reddish brown powder was collected by filtration. Anal. Calcd for **L10CuO_2**·0.5CH_2Cl_2, $C_{48.5}H_{71}N_6BCuO_2Cl$: C, 66.20; H, 8.13; N, 9.55; Found: C, 65.87; H, 8.19; N, 9.53. UV−vis (CH_2Cl_2, −78 °C): 452 nm (ϵ, 300 M^{-1} cm^{-1}), 700 nm (sh, 40), 975 nm (20). FTIR (cm^{-1}, KBr): ν(BH) 2540; ν(O−O) 1058 (ν(^{18}O−^{18}O) 1008), ν(Cu−O) 542 (ν(Cu−^{18}O) 518). Resonance Raman (cm^{-1}, CH_2Cl_2, 77 K, 482.5 nm ext): ν(O−O) 1043 (ν(^{18}O−^{18}O) 984). ^{1}H NMR (δ/ppm, CD_2Cl_2, 500 MHz, −78 °C): 1.18 (d, br, 18H, CH*Me*$_2$), 1.75−2.15 (complex m, br, 45H, Ad-*H*), 3.45 (m, br, 3H, C*H*Me$_2$), 6.06 (s, br, 3H, pz-*H*). This broad feature was due to low solubility of the obtained **L10CuO_2** at low temperature.

Magnetochemistry. Magnetic susceptibility data of L3CuO_2 were collected using a Quantum Design model MPMS SQUID magnetometer over a temperature range 50−250 K on the same batch of crystalline samples used for structural determination.[18] Data error bars were estimated on the basis of the scatter of the data in the low-temperature region. A small amount of paramagnetic S = $^1/_2$ impurity was subtracted. The data were analyzed using a Hamiltonian including the singlet/triplet energy splitting and Zeeman terms.

Physical Methods. Low-temperature absorption spectroscopy was performed on a double beam spectrophotometer (Cary 500) using a liquid helium cryostat (Janis Research Super Vari-Temp) or on an Otsuka Electronics MCPD-2000 system with an optical fiber attachment (300−1100 nm) using NESLAB CB-80. ^{1}H NMR spectra were collected on a Bruker AVANCE-500 (500 MHz) or a JEOL EX-400 (400 MHz) spectrometer. Mull absorption samples were prepared by dispersing the grounded powder of the complexes in poly(dimethylsiloxane) (Aldrich) or mineral oil (Mallinckrodt) and sandwiching them between two quartz disks in a homemade sample holder. Resonance Raman (rR) spectra were obtained using a series of lines from Kr^+ (Coherent 190C-K) and Ar^+ (Coherent Sabre 25/7) ion lasers with incident power ranging from 5 to 20 mW in an ~135° backscattering configuration. Scattered light was dispersed through a triple monochromator (Spex 1877 CP, with 1200, 1800, and 2400 groove/mm gratings) and detected with a back-illuminated CCD camera (Princeton

(23) George, S. D.; Fujisawa, K.; Solomon, E. I., unpublished results.
(24) Note an alternative description of Cu^{II}-superoxo is the isoelectronic Cu^{III}-peroxo description, which, however, would have very different electronic/spectroscopic properties, that is, different d−d transition energies due to the +3 oxidation state of Cu and a much lower O−O vibrational frequency.
(25) Baldwin, M. J.; Root, D. E.; Pate, J. E.; Fujisawa, K.; Kitajima, N.; Solomon, E. I. *J. Am. Chem. Soc.* **1992**, *114*, 10421.
(26) The detailed synthetic methods and their properties will be described in a separate paper.

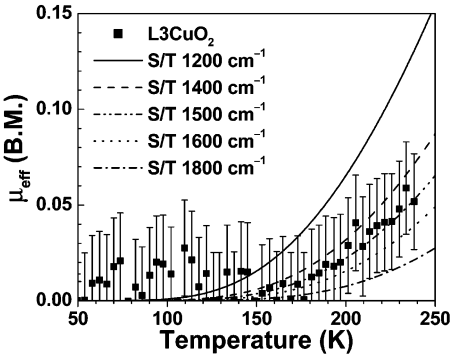

Figure 2. SQUID measured effective magnetic moment μ_{eff} (B.M. = Bohr magneton) of $L3CuO_2$. Lines are the simulated curves assuming the S/T energy splitting ($E_{S=1} - E_{S=0}$) = 1800, 1600, 1500, 1400, or 1200 cm^{-1}.

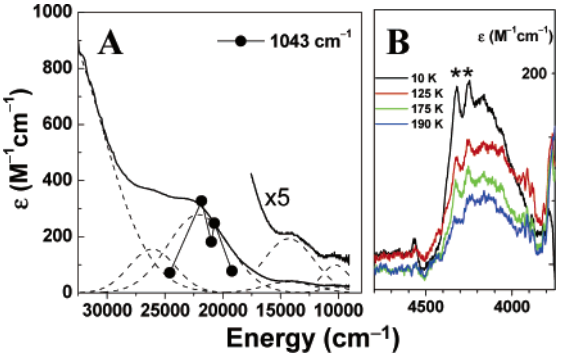

Figure 3. (A) UV/vis absorption spectrum of $L10CuO_2$ in CH_2Cl_2 at −70 °C (solid line) with Gaussian resolved individual transitions (dashed lines). Overlaid is the rR profile of the 1043 cm^{-1} vibrational mode of $L10CuO_2$ (●). (B) Variable temperature near-IR mull absorption spectra of $L10CuO_2$. Vibrational overtones of the mulling agent are labeled as "*".

Instruments ST-135). The samples contained in NMR tubes were immersed in a liquid nitrogen finger dewar. Raman peak intensities were referenced to the CH_2Cl_2 solvent peaks for excitation profiles. IR and far-IR spectra were recorded in a solid KBr disk and a solid CsI disk, respectively, on a JASCO-550 spectrometer. Elemental analyses were determined at an analytical facility at the Research Laboratory of Resources Utilization, Tokyo Institute of Technology, and the Chemical Analysis Center of the University of Tsukuba.

Electronic Structure Calculations. Density functional theory (DFT) calculations were performed on a PC cluster and a SGI Origin 2000 workstation. ADF 2.01[27] was used for ground-state and excited-state calculations where the Cu nuclear charge is adjusted ($Z = +28.55$) according to previous DFT studies using $CuCl_4^{2-}$ as calibration.[28] Local density approximation of Vosko, Wilk, and Nusair[29] and the nonlocal gradient corrections of Becke[30] and Perdew[31] were used. A triple-ζ Slater-type orbital basis set with a single polarization function (ADF basis set IV) was used in all ADF calculations. Core orbitals were frozen through 3p (Cu) and 1s (O, C, N, B). Gaussian 98[32] was used for functional dependence studies of the DFT calculations. Pure density functional BP86, hybrid functional B3LYP, and a spectroscopically calibrated hybrid functional B38HFP86 (38% Hartree−Fock exchange added to the BP86 functional[28]) were used. A general basis set (6-311G* for Cu and 6-31G* for all other atoms) was used for all Gaussian calculations, and results were analyzed using AOMix.[33] The model coordinates for calculations were taken from the crystal structure of $Cu(O_2)[HB(3\text{-}^tBu\text{-}5\text{-}^iPrpz)_3]$.[18] Alkyl side chains on the pyrazole rings of the ligand were replaced by hydrogen atoms.

3. Results and Analysis

3.1. Magnetism and Spectroscopy. 3.1.1. Magnetochemistry. Figure 2 gives the temperature dependence of the effective molecular magnetic moment μ_{eff} of $L3CuO_2$ taken on the same batch of crystalline solid used for crystal structure determination.[18] The purity of the sample is confirmed by the crystallographic characterization and elemental analysis (see Experimental Section). The μ_{eff} is almost zero at low temperature (<150 K), confirming the diamagnetic singlet ground state ($S = 0$) of the molecule ($\mu_{eff} \approx 2.83\ \mu_B$ for the $S = 1$ state). The μ_{eff} deviates slightly from zero at higher temperatures, and this deviation is not present in control experiments on pure diamagnetic materials, suggesting the presence of a low-lying triplet excited state ($S = 1$) with a small thermal population. The magnetic properties of $L3CuO_2$ could be analyzed using the Bleaney and Bowers equation $\chi = (2Ng^2\beta^2/kT)/[3 + \exp(\Delta_{S/T}/kT)]$, where $\Delta_{S/T}$ is the singlet/triplet (S/T) energy splitting ($\Delta_{S/T} = E_{S=1} - E_{S=0}$), and $\mu_{eff} = (3\chi kT/N\beta^2)^{1/2}$.[34] The best fit to the data estimates a low-lying excited triplet state at 1500 ± 300 cm^{-1} above the singlet ground state (Figure 2).

3.1.2. Electronic Absorption. The previously reported $L3CuO_2$ solution absorption spectrum shows a band at ~350 nm (~28 800 cm^{-1}) with $\epsilon \approx 2330\ M^{-1}\ cm^{-1}$ (Figure S1A).[18] This absorption band is in fact from a dimeric $L3Cu^{II}(O_2)Cu^{II}$-L3 component, which has an intense charge-transfer absorption band at ~350 nm with $\epsilon > 20\,000\ M^{-1}\ cm^{-1}$ obscuring the Cu^{II}-superoxo spectral features.[25] The presence of this dimer component was identified by the rR spectra on the solution samples of $L3CuO_2$ excited at 363.8 nm (~27 500 cm^{-1}), which show an intense Cu−Cu vibrational mode at 308 cm^{-1}, characteristic of the side-on peroxo dimer (Figure S1B).[35] This component is not present in the solid sample used for the magnetic susceptibility measurements, which came from the crystalline solid used for crystallographic characterization.[18] To avoid this dimer component in solution, the analogous complex $Cu(O_2)[HB(3\text{-Ad-}5\text{-}^iPrpz)_3]$ ($L10CuO_2$) was synthesized. Its absorption spectrum indicates that the much bulkier adamantyl ligand prevents dimerization in solution.

The UV/vis solution absorption spectrum of $L10CuO_2$ in CH_2Cl_2 is presented in Figure 3A.[36] No intense absorption band is present, and four weak transitions are observed at 10 200,

(27) *Amsterdam Density Functional (ADF)*, 2.0.1; Theoretical Chemistry, Vrije Universiteit: Amsterdam, 1995.
(28) Szilagyi, R. K.; Metz, M.; Solomon, E. I. *J. Phys. Chem. A* **2002**, *106*, 2994.
(29) Vosko, S. H.; Wilk, L.; Nusair, M. *Can. J. Phys.* **1980**, *58*, 1200.
(30) Becke, A. D. *J. Chem. Phys.* **1986**, *84*, 4524.
(31) Perdew, J. P. *J. Chem. Phys.* **1986**, *33*, 8822.
(32) Frisch, M. J.; Trucks, G. W.; Schlegel, H. B.; Scuseria, G. E.; Robb, M. A.; Cheeseman, J. R.; Zakrzewski, V. G.; Montgomery, J. A., Jr.; Stratmann, R. E.; Burant, J. C.; Dapprich, S.; Millam, J. M.; Daniels, A. D.; Kudin, K. N.; Strain, M. C.; Farkas, O.; Tomasi, J.; Barone, V.; Cossi, M.; Cammi, R.; Mennucci, B.; Pomelli, C.; Adamo, C.; Clifford, S.; Ochterski, J.; Petersson, G. A.; Ayala, P. Y.; Cui, Q.; Morokuma, K.; Malick, D. K.; Rabuck, A. D.; Raghavachari, K.; Foresman, J. B.; Cioslowski, J.; Ortiz, J. V.; Baboul, A. G.; Stefanov, B. B.; Liu, G.; Liashenko, A.; Piskorz, P.; Komaromi, I.; Gomperts, R.; Martin, R. L.; Fox, D. J.; Keith, T.; Al-Laham, M. A.; Peng, C. Y.; Nanayakkara, A.; Gonzalez, C.; Challacombe, M.; Gill, P. M. W.; Johnson, B.; Chen, W.; Wong, M. W.; Andres, J. L.; Gonzalez, C.; Head-Gordon, M.; Replogle, E. S.; Pople, J. A. *Gaussian 98*, revision A.7; Gaussian, Inc.: Pittsburgh, PA, 1998.
(33) Gorelsky, S. I.; Lever, A. B. P. *AOMix program*, revision 4.7; York University: Ontario, Canada, 2001.
(34) Kahn, O. *Molecular Magnetism*; VCH Publishers: New York, 1993.
(35) This $L3Cu^{II}(O_2)Cu^{II}L3$ dimeric component also exists in the solutions of the monomeric hydroperoxo complex $L3Cu^{II}OOH$, which was prepared independently by reacting $L3Cu^{II}OH$ with H_2O_2. The characteristic Raman features of $L3Cu^{II}(O_2)Cu^{II}L3$ were observed. (See: Chen, P.; Fujisawa, K.; Solomon, E. I. *J. Am. Chem. Soc.* **2000**, *122*, 10177.)
(36) The mull UV/vis absorption spectrum of $L10CuO_2$ is very similar to that of the solution (Figure S2).

Scheme 1. Schematic Diagram of the Interaction between the Cu^{II} d_{xy} and Superoxide π^*_σ/π^*_v Orbitals[a]

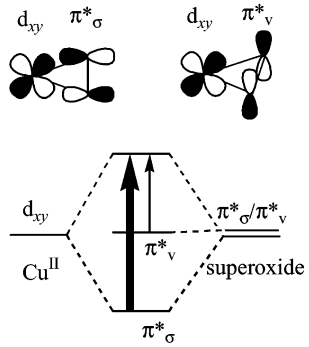

[a] The arrows and their widths indicate the expected CT transitions and their relative intensities.

14 300, 22 100, and 26 100 cm^{-1} with extinction coefficients all <400 M^{-1} cm^{-1}. These bands are assigned as Cu^{II} d−d transitions on the basis of their low extinction coefficients. Their energies are similar to those of ligand field transitions of square pyramidal Cu^{II} complexes.[37] The onset of an intense absorption band occurs at energies $>30\,000$ cm^{-1}.

Calculations predicted the presence of an additional low-lying singlet excited state ($<10\,000$ cm^{-1}, see section 3.2.1). Therefore, the absorption measurement of $L10CuO_2$ was extended into the near-IR region. A mull sample was used to avoid the strong vibrational overtone absorption of solvents. An electronic transition is observed at 4200 cm^{-1} with $\epsilon \approx 200$ M^{-1} cm^{-1} (Figure 3B).[38] This low energy transition is not present in the thermodecomposed product, which is the Cu^{I} complex resulting from loss of the coordinated superoxide as dioxygen. This transition is also not observed for the bis(μ-OH) bridged dimeric $L1Cu^{II}(OH)_2Cu^{II}L1$ complex (L1 = [HB(3,5-^{i}Prpz)$_3$], hydrotris-(3,5-diisopropyl-1-pyrazolyl)borate), which has a similar five-coordinate Cu^{II} with the hydrotris(pyrazolyl)borate ligand (Figure S4).[39] This excludes the possibility of this transition being a broad vibrational overtone envelope of the hydrotris-(pyrazolyl)borate ligand and indicates it is an electronic transition associated with the superoxide complex. The electronic nature of this transition is further supported by the broadening in its bandwidth and the decrease in amplitude at high temperature due to the Franck−Condon factor in absorption[40] and the decreased excited-state lifetime from efficient vibrational relaxation for low energy electronic excited states (Figure 3B).[41−43]

For Cu^{II} in a square pyramidal geometry, the highest Cu d orbital is the *xy* orbital (see Figure 1 for molecular coordinate definition). The highest occupied orbitals of the superoxide are the doubly degenerate orthogonal π^* orbitals (Scheme 1, π^*_σ and π^*_v), which contain a total of three electrons. The π^*_σ orbital of the superoxide is in the CuO_2 plane and has good overlap and thus a strong bonding interaction with the Cu *xy* orbital. This would result in an intense superoxide π^*_σ to Cu *xy* charge-transfer (CT) transition (Scheme 1). Experimentally, no intense absorption band is observed in the UV/vis/near-IR region, which puts a lower energy limit of 32 500 cm^{-1} for the superoxide π^*_σ to Cu *xy* CT excited state (Figure 3). The superoxide π^*_v orbital is perpendicular to the Cu *xy* orbital and should not undergo a strong bonding interaction with the Cu (Scheme 1). The low energy of the 4200 cm^{-1} band excludes the possibility of its assignment as a Cu^{II} ligand-field transition.[37] Its connection with the presence of superoxide ligation suggests its assignment as the π^*_v to Cu *xy* CT transition. Its low intensity is consistent with the poor overlap between the π^*_v and Cu *xy* orbitals. Because the superoxide π^*_v and the Cu *xy* orbitals are orthogonal to each other, their interaction should thus lead to a triplet state lower in energy. Therefore, the thermally accessible low-lying triplet state at $\sim$1500 cm^{-1} observed in the magnetic susceptibility measurement can be assigned as the π^*_v to Cu *xy* CT triplet state. Consequently, the ground-state singlet of the Cu^{II}-superoxo complex does not result from the interaction between the Cu *xy* and superoxide π^*_v orbitals and must derive from an electronic interaction different from the lowest triplet state. (The nature of the ground-state singlet will be considered in section 3.2.1.)

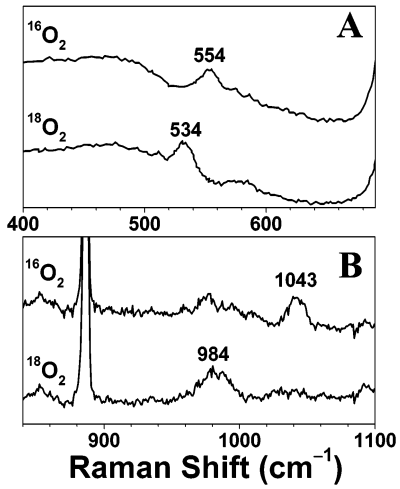

Figure 4. Resonance Raman spectra of $L3CuO_2$ excited at 406.7 nm ($\sim$24 590 cm^{-1}) (A), and $L10CuO_2$ excited at 482.5 nm ($\sim$20 725 cm^{-1}) (B) in CH_2Cl_2.

3.1.3. Vibrational Spectroscopy. The IR spectrum of the $L3CuO_2$ complex shows the superoxide O−O vibration at 1112 cm^{-1}, which shifts to 1060 cm^{-1} upon 18-oxygen substitution (Figure S3).[18] The previously reported rR O−O vibration of $L3CuO_2$ at 1111 cm^{-1} is in fact due to the side-on peroxo dimer $L3Cu(O_2)CuL3$ component in solution, which has a broad vibrational overtone at 1097 cm^{-1} with a similar 18-O isotope shift and obscures the superoxide O−O vibration (Figure S1B). (Note that this dimer overtone is not active in IR due to its g symmetry.) Another IR vibrational feature at 550 cm^{-1} shifts to 532 cm^{-1} upon 18-oxygen labeling (Figure S3) and is also observed in the resonance Raman spectrum at 554 cm^{-1} (534 cm^{-1} in the 18-oxygen labeled sample, Figure 4A). This vibrational mode is assigned as the symmetric Cu−O stretch

(37) Lever, A. B. P. *Inorganic Electronic Spectroscopy*, 2nd ed.; Elsevier Science: Amsterdam, The Netherlands, 1984.
(38) The extinction coefficients here were obtained by correlating the mull absorption spectrum to the solution spectrum in the UV/vis region.
(39) Kitajima, N.; Fujisawa, K.; Fujimoto, C.; Moro-oka, Y.; Hashimoto, S.; Kitagawa, T.; Toriumi, K.; Tatsumi, K.; Nakamura, A. *J. Am. Chem. Soc.* **1992**, *114*, 1277.
(40) Hitchman, M. A.; Riley, M. J. In *Inorganic Electronic Structure and Spectroscopy*; Solomon, E. I., Lever, A. B. P., Eds.; John Wiley & Sons: New York, 1999; Vol. 1.
(41) Henderson, B.; Imbush, G. F. *Optical Spectroscopy of Inorganic Solids*; Clarendon Press: Oxford, 1989.
(42) Clark, R. J. H.; Dines, T. J. In *Advances in Infrared and Raman Spectroscopy*; Clark, R. J. H., Hester, R. E., Eds.; London, 1982; Vol. 9, p 282.
(43) Halperin, B.; Nicollin, D.; Koningstein, J. A. *Chem. Phys.* **1979**, *42*, 277.

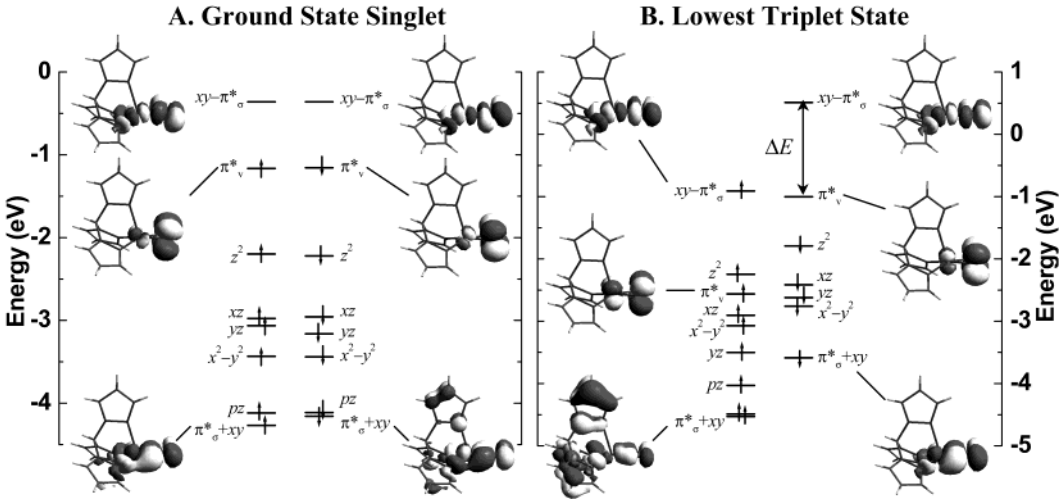

Figure 5. Energy level diagrams and selected MO surface contours of the ground-state singlet (A) and the lowest triplet state (B) from the spin-unrestricted DFT calculations in ADF; pz: pyrazole ligand.

on the basis of its frequency and isotope shift.[44] The O−O vibration is observed in the L10CuO_2 resonance Raman spectrum at 1043 cm^{-1} and shifts to 984 cm^{-1} upon 18-oxygen labeling (Figure 4B).[45] A normal coordinate analysis[46] on the CuO_2 core using the L3CuO_2 vibrational data and a general valence force field[47] yields the force constant $k_{O-O} = 5.72$ mdyn/Å, typical of a superoxide O−O bond (Table S1).[22]

The resonance Raman profile of the L10CuO_2 O−O vibration is included in Figure 3A. It has slight resonance enhancement over the 22 100 cm^{-1} band in the absorption spectrum. This indicates excited-state geometric distortion along the O−O bond and thus some superoxide π^* to Cu CT mixing into this d−d transition. The *yz* orbital is the only Cu d orbital with the correct symmetry to mix with the superoxide π^* orbitals in the C_s point group (Figure 1) in the excited states, which enables the assignment of the 22 100 cm^{-1} band as the Cu^{II} *yz* → *xy* transition.

3.2. Calculations. 3.2.1. Electronic Structure Description: Nature of Singlet/Triplet States. Spin-unrestricted density functional calculations were performed on a model complex derived from the L3CuO_2 crystal structure (see Experimental Section), to correlate with the spectroscopic results to gain more insight into the electronic structure of the Cu^{II}-superoxo complex. The energy level diagrams and selected MO surface contours of the calculated singlet ground state and lowest triplet state are presented in Figure 5 A and B. Table 1 summarizes the energies and compositions of selected spin-down MOs. Additional MO energies and compositions are given in Tables S2 and S3.[48]

Table 1. Energies (eV) and Compositions (%) of Spin-Down Cu d and Superoxide π^*-Based MOs from the Spin-Unrestricted DFT Calculations (ADF) of the Singlet Ground State and the Lowest Triplet State

singlet ground state				lowest triplet state			
level	*E*	Cu	O_2	level	*E*	Cu	O_2
$xy-\pi^*_\sigma$	−0.359	35	57	$xy-\pi^*_\sigma$	0.509	50	40
π^*_v	−1.157	10	87	π^*_v	−1.003	12	86
z^2	−2.221	82	2	z^2	−1.793	85	2
xz	−2.956	88	5	*xz*	−2.415	90	4
yz	−3.163	76	9	*yz*	−2.620	72	16
x^2-y^2	−3.439	82	4	x^2-y^2	−2.758	84	3
$\pi^*_\sigma+xy$	−4.158	33	32	$\pi^*_\sigma+xy$	−3.588	38	51
spin density		−0.001	0.006	spin density		0.611	1.300

The calculated ground state is a diamagnetic singlet state (Figure 5A) as experimentally observed (section 3.1.1). All spin-allowed electronic excitations from this ground state involve promoting an electron from an occupied MO to the LUMO of the same spin. We focus our analysis on the spin-down set, which is representative of both spin manifolds (Figure 5A, right, Table 1). The calculated spin-down LUMO of the ground state is the Cu *xy* orbital, which has a strong antibonding interaction with the superoxide π^*_σ orbital (labeled $xy-\pi^*_\sigma$, Figure 5A). The superoxide π^*_v level is situated higher in energy than all of the Cu d levels except *xy* and forms the HOMO, predicting a low-lying π^*_v to Cu *xy* CT singlet excited state. Tetragonal Cu^{II} complexes with innocent ligands do not have ligand field transitions below ∼10 000 cm^{-1}.[37] Thus, the transition observed in the L10CuO_2 absorption spectrum at 4200 cm^{-1} can be associated with this low-lying singlet excited state (Figure 3B). The intensity of this transition ($\epsilon \approx 200$ M^{-1} cm^{-1}) is consistent with the poor donor/acceptor orbital overlap between π^*_v and $xy-\pi^*_\sigma$.[49] The four Cu d levels lie below the superoxide π^*_v level. The Cu *yz* has the largest mixing with the superoxide π^*

(44) The asymmetric Cu−O vibration of the CuO_2 core is not resonance Raman active. Also, the dimeric side-on peroxo component in solution does not have a rR feature in this region. See ref 25.
(45) The different O−O vibrational frequency of L10CuO_2 and the L3CuO_2 might be due to the increased ligand strain associated with the bulky adamantyl side chain.
(46) Three internal coordinates (two r_{Cu-O} and one r_{O-O}) were included in the normal coordinate analysis on the CuO_2 three-atom model in C_{2v} symmetry. Two different diagonal force constants (k_{Cu-O}, k_{O-O}) were included. The introduction of an off-diagonal force constant between the two Cu−O modes is equivalent to increasing k_{Cu-O} by the same amount. (See: Neese, F.; Solomon, E. I. *J. Am. Chem. Soc.* **1998**, *120*, 12829.) This off-diagonal force constant is thus set to zero. An off-diagonal force constant ($k_{Cu-O/O-O}$) between the Cu−O and O−O stretch has a limited effect on the predicted isotope shifts of the two totally symmetric vibrational modes. Varying this interaction force constant between −0.1 and 0.1 mdyn/Å does not improve the fit. The force constants reported here were from an analysis using $k_{Cu-O/O-O} = 0$ mdyn/Å.
(47) McIntosh, D. F.; Michaelian, K. H.; Peterson, M. R. *Can. J. Chem.* **1978**, *56*, 1289.
(48) A general electronic structure model for d^6/d^7 metal-superoxo/peroxo complexes was described by Lever and Gray. (*Acc. Chem. Res.* **1978**, *11*, 348.) The spectroscopic predictions for the d^9 Cu^{II}-superoxo complex studied here are different from those of d^6/d^7 metals due to the presence of only one hole on the Cu atom.
(49) Solomon, E. I. *Comments Inorg. Chem.* **1984**, *3*, 227.

Table 2. Excited Singlet ($^1\Gamma$) and Triplet ($^3\Gamma$) State Energies (cm^{-1}) from Spin-Unrestricted DFT Calculations in ADF on the Cu^{II}-Superoxo Complex[a]

state	*E*	state	*E*
$^1\Gamma(xy-\pi^*_\sigma)$	0		
$^1\Gamma(\pi^*_v)$	5515	$^3\Gamma(\pi^*_v)$	2385
$^1\Gamma(z^2)$	21 025	$^3\Gamma(z^2)$	18 130
$^1\Gamma(x^2-y^2)$	25 420	$^3\Gamma(x^2-y^2)$	23 505
$^1\Gamma(xz)$	25 505	$^3\Gamma(xz)$	23 100
$^1\Gamma(yz)$	27 760	$^3\Gamma(yz)$	21 365
$^1\Gamma(\pi^*_\sigma+xy)$	34 610	$^3\Gamma(\pi^*_\sigma+xy)$	26 430

[a] States are labeled by the donor orbitals of the corresponding electronic transitions.

orbitals (Table 1), consistent with the observed weak rR enhancement of the L10CuO$_2$ O−O vibration by the absorption band at 22 100 cm^{-1}, which is assigned as the Cu *yz* → *xy* transition (Figure 3A, section 3.1.3). The superoxide π^*_σ level is calculated to be at deeper energy than all Cu d levels. The corresponding intense (due to large donor/acceptor overlap) π^*_σ to Cu *xy* CT transition is at energies >32 500 cm^{-1} from experiment (section 3.1.2).

The calculated singlet ground-state MO energy diagram is in good qualitative agreement with the spectroscopic results (Figures 5A and 3). ΔSCF excited-state calculations were performed to obtain quantitative singlet−singlet transition energies.[50] The calculated transition energies are in reasonable agreement with experiment with π^*_v CT < d−d < π^*_σ CT (Table 2 and Figure 3). The superoxide π^*_v to Cu CT state is calculated to be the lowest singlet excited state at 5515 cm^{-1}, as predicted from the ground-state MO diagram and confirmed by experiment (4200 cm^{-1}, Figure 3B). The π^*_σ to Cu CT state is calculated to be at 34 610 cm^{-1}, consistent with the experimentally estimated lower limit of 32 500 cm^{-1} (section 3.1.2). The calculated d−d transition energies are higher than those experimentally observed, and the *yz* → *xy* transition, which is the second highest from experiment, is calculated to be highest in energy among the four d−d transitions.

Because both spin-up and spin-down LUMOs of the ground-state singlet are the Cu $xy-\pi^*_\sigma$ orbitals (Figure 5A), this singlet ground state correlates formally to a MO bonding scheme between Cu^{II} with a spin in its *xy* orbital and a superoxide ligand with its spin in the π^*_σ orbital (Scheme 2A). The two spin orbitals have large overlap and thus a large splitting between the bonding and antibonding molecular orbitals, resulting in the singlet state lowest in energy. Importantly, the calculated ground-state spin distributions have very little polarization (−0.001 spin on Cu and 0.006 spin on the superoxide, Table 1), indicating a highly covalent spin delocalized state. This is in contrast to a normal picture of a Cu^{II}−superoxide bond, where the spins on Cu^{II} and the superoxide are described as antiferromagnetically exchange coupled, that is, opposite spin density localized on Cu^{II} and on the superoxide. The implication of this spin delocalization versus the spin polarization of antiferromagnetic coupling will be discussed.

(50) Electronic excited states are calculated by promoting an electron from the donor orbital to the LUMO, within either the spin-up or the spin-down set, and converging the wave function at the excited states. The transition energies were calculated from the total energy difference between the ground and excited states. The DFT calculated excited-state wave function is actually a $M_s = 0$ state, contaminated by the $M_s = 0$ component of the corresponding $S = 1$ triplet state. Therefore, the excited $S = 1$ triplet states were calculated, and the $S = 0$ excited-state energies were determined using equation $[E(S = 1) - E(S = 0)]/2 = E(S = 1) - E(M_s = 0)$ as if localized.

Scheme 2. Bonding Schemes between Cu^{II} *xy* and Superoxide π^*_σ and π^*_v

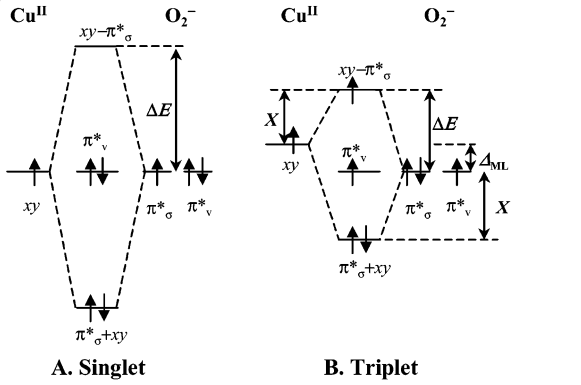

The calculated lowest triplet state is the π^*_v to Cu CT triplet state at 2385 cm^{-1} higher in energy than the ground-state singlet (Table 2 and Figure 5B). This triplet state can be associated with the thermally populated triplet state observed in the magnetic susceptibility experiment (Figure 2). The calculated ground-state singlet/triplet splitting is in reasonable agreement with the SQUID measured value (∼1500 cm^{-1}). The spin-down LUMO and LUMO+1 in the triplet MO diagram correspond to the two singly occupied MOs in a spin-restricted representation and indicate that this triplet state has one unpaired electron in the superoxide π^*_v orbital and the other one in the Cu $xy-\pi^*_\sigma$ orbital (Figure 5B). This state thus formally correlates to a MO bonding scheme between the Cu^{II} atom with a spin in its *xy* orbital and a superoxide ligand with its spin in its π^*_v orbital (Scheme 2B). The two spin orbitals are orthogonal to each other, resulting in a triplet state lower in energy than that of the corresponding singlet.

Consequently, the ground singlet state and the lowest triplet state are fundamentally different in nature, and the measured S/T splitting is not 2*J* as normally used for two localized interacting spins. These two states relate to each other through transfer of one electron between the π^*_v and $xy-\pi^*_\sigma$ orbitals, formally a charge-transfer process. The spin distribution of the singlet ground state is highly delocalized with no spin polarization in contrast to an antiferromagnetic coupling description of its diamagnetism.

3.2.2. Effect of Functional on Spin Polarization. In past studies, it has been found that the extent of spin delocalization can be dependent on the functional chosen.[28] The density functional used above is BP86 in the ADF program. In this section, the density functional is systematically varied by increasing the amount of Hartree−Fock (HF) exchange using a hybrid density functional approach in the Gaussian 98 package. The functionals used include BP86, B3LYP, and B38HFP86,[28] which contain 0, 20, and 38% HF exchange, respectively. The results obtained on the L3CuO$_2$ crystal structure derived model complex are summarized in Table 3. The calculated MO energy level diagrams and selected MO surface contour plots are given in Figures S5, S6, and S7.

At the pure density functional limit (BP86), the calculated lowest singlet and triplet states of the Cu^{II}-superoxo complex are similar to the results obtained from ADF calculations (Figures S5 and 5). The triplet state is higher in energy than the singlet with a S/T splitting of 643 cm^{-1}, qualitatively

Table 3. Density Functional Dependence of the Calculations on the Cu^{II}-Superoxo Complex

	BP86	B3LYP	B38HFP86
S/T splitting (cm^{-1})[a]	643	−1844	−4882
singlet spin distribution[b]	Cu: −0.01; O_2: 0.01	Cu: −0.02; O_2: 0.03	Cu: −0.54; O_2: 0.60
$\Delta E(xy-\pi^*_\sigma/\pi^*_v)$ (eV)[c]	1.10	0.94	0.81
$xy-\pi^*_\sigma$ composition[d]	43% Cu^{II}, 47% O_2^-	51% Cu^{II}, 40% O_2^-	59% Cu^{II}, 33% O_2^-
π^*_v composition[d]	6% Cu^{II}, 94% O_2^-	2% Cu^{II}, 98% O_2^-	1% Cu^{II}, 99% O_2^-

[a] S/T = *E*(triplet) − *E*(singlet). [b] Spin densities on the Cu atom and the superoxide of the lowest singlet state. [c] Spin-down $xy-\pi^*_\sigma/\pi^*_v$ (LUMO+1/LUMO) orbital energy splitting of the lowest triplet state. [d] Spin-down $xy-\pi^*_\sigma$ and π^*_v orbital compositions of the lowest triplet state.

consistent with experiment (Figure 2, Table 3).[51] Upon including HF exchange in the functional (B3LYP and B38HFP86), we found that the triplet state is increasingly stabilized and drops below the singlet state (S/T < 0, Table 3), to become the ground state ($S = 1$, paramagnetic). Concomitant with this, the singlet state becomes more spin polarized. Opposite spin densities localize on the Cu and the superoxide (Cu: −0.54 spin, superoxide: 0.60 spin, in the B38HFP86 calculation, Table 3), leading to a singlet state where the interaction is reasonably described as an antiferromagnetic exchange coupled system. Additionally, the Cu d manifold shifts to lower energy and drops below the superoxide π^*_σ level as the HF exchange is increased in the density functional calculations (Figures S6 and S7).

Because the lowest singlet and triplet states involve different bonding interactions between the Cu^{II} and the superoxide (Scheme 2), the molecular geometries could be different for these two states. (The $L3CuO_2$ crystal structure is associated with the singlet state geometry, which is used for the above calculations.) To account for the possible effect of different geometries on the relative energies of the singlet and the triplet states, geometry optimizations were also performed for both states with different functionals. Table 4 summarizes the optimized geometries, calculated S/T splitting, and the singlet spin distributions. The calculated O−O bond of the singlet is longer than that in the $L3CuO_2$ crystal structure with all three functionals. Within each functional, the O−O bond at the triplet state is slightly shorter than that at the singlet state, while the Cu−O bond is longer. This is consistent with their different bonding interactions because the triplet state derives formally from a superoxide $\pi^*_v \rightarrow xy-\pi^*_\sigma$ CT process from the singlet state (Scheme 2). This CT process moves electron density from a mainly superoxide O−O antibonding orbital (π^*_v) to a mainly Cu−O antibonding orbital ($xy-\pi^*_\sigma$) and thus leads to the shortened O−O and elongated Cu−O bond in the triplet state. The calculated S/T splitting with geometry optimizations shows the same trend and similar magnitudes as those obtained in the above calculations based on the crystal structure. At the pure density functional limit (BP86), the singlet is the ground state, and the triplet is 742 cm^{-1} higher in energy (Table 4), qualitatively consistent with experiment (Figure 2, Table 3). With increasing HF exchange included in the functional, the triplet state drops below the singlet state (S/T < 0) to become the ground state. The singlet state concomitantly becomes more spin polarized with opposite spin densities localized on the Cu and the superoxide (Cu: −0.59 spin, superoxide: 0.68 spin, in the B38HFP86 calculations, Table 4), corresponding more to an antiferromagnetic exchange coupled system.

Scheme 3

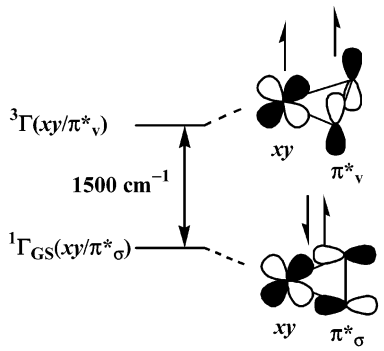

The magnetic susceptibility data in Figure 2 show that the ground state of the Cu^{II}-superoxo complex is a diamagnetic singlet state with the lowest triplet state ~1500 cm^{-1} higher in energy (section 3.1.1). The electronic absorption spectrum (Figure 3) indicates that the Cu d manifold is above the superoxide π^*_σ level in energy (section 3.1.2). Correlating these experimental results with the results obtained with different density functionals indicates that the pure density functional BP86 gives the most reasonable description of the electronic structure of the Cu^{II}-superoxo complex. The ground-state singlet in the pure DFT calculation is highly delocalized with no spin localization (Tables 3 and 4), consistent with the results obtained in section 3.2.1 and indicating that an antiferromagnetic coupled description is not appropriate for the ground-state diamagnetism of the Cu^{II}-superoxo complex.

4. Discussion

A combination of spectroscopic characterization and DFT calculations has provided a detailed electronic structure description of the monomeric side-on Cu^{II}-superoxo complex. The Cu^{II}-superoxo complex has a diamagnetic singlet ground state and a low-lying triplet state at ~1500 cm^{-1} higher in energy. The singlet ground state involves a strong interaction between the Cu *xy* and the superoxide π^*_σ orbital (Scheme 3, bottom). The lowest triplet state involves the interaction between the orthogonal Cu *xy* and the superoxide π^*_v orbital and has a fundamentally different orbital configuration from the ground-state singlet (Scheme 3, top). This triplet state is related to the ground-state singlet through a superoxide π^*_v to Cu *xy* CT process (Scheme 2), and the corresponding π^*_v excited singlet state is observed at 4200 cm^{-1} in the electronic absorption spectrum (Figure 3B).

The relative energy of the π^*_v triplet state to the π^*_σ singlet ground state is related to the splitting (ΔE) of the two singly occupied molecular orbitals in a spin-restricted representation ($xy-\pi^*_\sigma$ and π^*_v, Scheme 2B), which correspond to the spin-down LUMO+1/LUMO ($xy-\pi^*_\sigma/\pi^*_v$) in the spin-unrestricted description (see Figure 5B). Decreasing the $xy-\pi^*_\sigma/\pi^*_v$ splitting, ΔE, will stabilize the triplet state which eventually becomes the ground state, whereas a large ΔE will destabilize the triplet and eventually overcome the electron repulsion for spin pairing leading to the π^*_σ singlet ground state (Scheme 2A). This trend is reflected in singlet/triplet state ordering calculated using

(51) The difference in calculated ground-state S/T splitting between the ADF and Gaussian 98 calculations is probably due to the different basis set functions used in the two programs (Gaussian 98, Gaussian type orbitals; ADF, Slater type orbitals) and the frozen core approximation used in ADF.

Table 4. Optimized Geometries for Both Singlet and Triplet States with Different Density Functionals on the Cu^{II}-Superoxo Complex

	BP86		B3LYP		B38HFP86	
	singlet	triplet	singlet	triplet	singlet	triplet
r(O−O) (Å)	1.362	1.326	1.356	1.311	1.325	1.295
r(Cu−O) (Å)	1.857	1.959	1.813	1.952	1.854	1.920
S/T splitting (cm^{-1})[a]	742		−2537		−4344	
singlet spin distribution[b]	Cu: −0.01; O_2: 0.01		Cu: 0.00; O_2: 0.00		Cu: −0.59; O_2: 0.68	

[a] S/T = E(triplet) − E(singlet). [b] Spin densities on the Cu atom and the superoxide of the lowest singlet state.

different functionals. The B38HFP86 calculations give a small $xy-\pi_\sigma^*/\pi_v^*$ splitting (ΔE = 0.81 eV, Table 3), leading to the triplet state lower than the singlet, contrary to the experimental result. Alternatively, the BP86 calculations give a larger splitting (ΔE = 1.10 eV, Table 3), and a ground-state singlet/triplet energy ordering consistent with experiment is obtained (calculated S/T = 643 cm^{-1}, Table 3, experimental S/T ≈ 1500 cm^{-1}).

The smaller $xy-\pi_\sigma^*/\pi_v^*$ splitting ΔE in the B38HFP86 calculation results from the increased HF exchange in the functional, which shifts the Cu d manifold up in energy relative to the superoxide π^* valence orbitals and thus increases their energy separation (Δ_{ML}, Scheme 2B).[28] From perturbation theory,[52] the increased Δ_{ML} would lead to a weakened interaction between the Cu xy and the superoxide π_σ^* orbital and thus reduce the magnitude of the antibonding orbital destabilization energy ($X \propto 1/\Delta_{ML}$, Scheme 2B). This is reflected in the covalency of the $xy-\pi_\sigma^*$ orbital, where the B38HFP86 calculation has more Cu character and is thus less covalent due to the increased Δ_{ML} (59% Cu + 33% O_2^-, Table 3). This results in a smaller $xy-\pi_\sigma^*/\pi_v^*$ splitting ΔE and the triplet as the ground state in the B38HFP86 calculation. Comparatively, the BP86 calculation gives a more covalent Cu xy and superoxide π_σ^* interaction (43% Cu + 47% O_2^-, Table 3), and thus ΔE is large enough to overcome the electron repulsion for spin pairing, leading to the singlet ground state (Scheme 2A, Table 3).

The strong covalent interaction between the Cu xy and the superoxide π_σ^* orbital also leads to a large separation of the corresponding bonding/antibonding orbitals ($xy-\pi_\sigma^*/\pi_\sigma^*+xy$, Scheme 2A). This gives rise to the high energy of the π_σ^* to Cu xy CT state. It also leads to a very high energy xy/π_σ^* triplet state, which correlates to an electron configuration having one spin-up electron in the $xy-\pi_\sigma^*$ and the second spin-up electron in the π_σ^*+xy orbital. This is formally a superoxide π_σ^* to Cu xy CT triplet state and is calculated to be at 26 430 cm^{-1} ($^3\Gamma(\pi_\sigma^*+xy)$, Table 2).

The energy separation of the $xy-\pi_\sigma^*$ and π_σ^*+xy molecular orbitals also affects the extent of spin polarization of the ground-state singlet.[53] These two MOs are linear combinations of interacting Cu xy and superoxide π_σ^* orbitals, each of which carries a single spin before interaction (Scheme 2A). From these two MOs, the many-electron configurations arise (Scheme 4, $\phi_1 \approx \pi_\sigma^*+xy$, $\phi_2 \approx xy-\pi_\sigma^*$).[53,54]

The lowest singlet state wave function of the system ψ_S will be a linear combination of S_1, S_2, and S_3:[55]

$$\psi_S = \lambda_1\psi_{S_1} + \lambda_2\psi_{S_2} + \lambda_3\psi_{S_3} \qquad (1)$$

while the triplet state is well represented by ψ_T. (Note that the triplet state here is fundamentally different from the lowest triplet state discussed above, which involves the superoxide π_v^* orbital.) When the energy separation of ϕ_1 and ϕ_2 is small (weak interaction limit), $|\lambda_1| \approx |\lambda_2| \approx |\lambda_3|$, and the strong mixing between S_1 and S_2 would lead to the ground-state wave function ψ_S highly polarized with opposite spin densities localized on the Cu and the superoxide, corresponding to an antiferromagnetically coupled singlet state. If the energy splitting of ϕ_1/ϕ_2 is large (strong interaction limit), $|\lambda_1| \gg |\lambda_2|, |\lambda_3|$, and the wave function ψ_S is delocalized with no spin polarization. This is the case for the mononuclear side-on superoxo-Cu^{II} complex. The highly covalent interaction between the Cu xy and superoxide π_σ^* orbitals leads to a large energy separation of ϕ_1 and ϕ_2, and the resulting ground-state singlet is highly delocalized with no spin polarization (Figure 6A). In contrast, the B38HFP86 calculation gives a less covalent interaction between the Cu xy and superoxide π_σ^* orbital and thus a smaller energy separation of ϕ_1 and ϕ_2. This leads to the calculated singlet state being highly spin polarized (Figure 6B) and an opposite singlet/triplet energy ordering as compared to experiment.

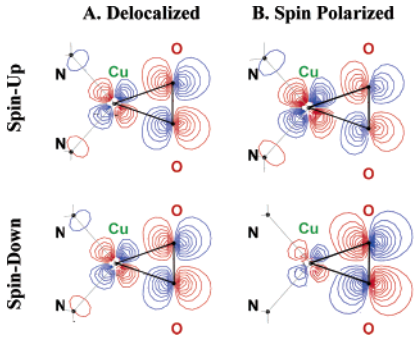

Figure 6. Two-dimensional CuO_2 plane $xy-\pi_\sigma^*$ MO contours from Gaussian 98 calculations. (A) Delocalized spin-up (top) and spin-down (bottom) $xy-\pi_\sigma^*$ orbitals of the Cu^{II}-superoxo complex from the unrestricted BP86 singlet state calculation. Both orbitals have similar Cu/O_2 characters (27% Cu + 66% O_2^-). (B) Polarized spin-up (top, 59% Cu + 31% O_2^-) and spin-down (bottom, 8% Cu + 88% O_2^-) $xy-\pi_\sigma^*$ orbitals from the unrestricted B38HFP86 singlet state calculation.

Scheme 4

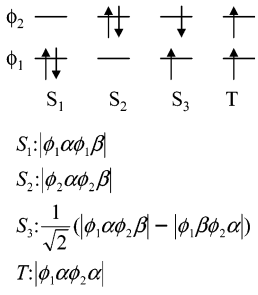

(52) Ballhausen, C. J.; Gray, H. B. *Molecular Orbital Theory*; W. A. Benjamin, Inc.: New York, 1964.

(53) Hay, P. J.; Thibeault, J. C.; Hoffman, R. *J. Am. Chem. Soc.* **1975**, *97*, 4884.
(54) Here, all MOs are from high-spin (triplet) calculations.
(55) Note here that S_1, S_2, and S_3 all have the same symmetry.

In summary, the diamagnetic singlet ground state of the mononuclear side-on superoxo-Cu^{II} complex results from the highly covalent interaction between the Cu *xy* and the superoxide π^*_σ orbitals. The large covalency leads to a singlet ground state with no spin polarization; thus, it is inappropriate to describe this as an antiferromagnetic coupled system. The lowest triplet state is fundamentally different in electronic origin from the ground-state singlet and involves the Cu *xy* and the superoxide π^*_v orbital. This π^*_v triplet is related to a very low energy singlet π^*_v CT transition at 4200 cm^{-1} above the ground-state singlet. Thus, the singlet/triplet splitting observed experimentally does not reflect antiferromagnetic exchange coupling, but rather a low energy charge-transfer process.

Acknowledgment. This research is supported by NIH Grant DK-31450 (E.I.S.) and JSPS Grant (13555257 and 14350471) (K.F.). We thank Dr. S. D. George for making available unpublished Cu K-edge data. K.F. is grateful to Ms. T. Kobayashi (Tokyo Institute of Technology) and Mr. N. Tada (University of Tsukuba) for preparing complexes and Prof. K. Okamoto (University of Tsukuba) for his encouragement. P.C. is a Gerhard Casper Stanford Graduate Fellow.

Supporting Information Available: $L3CuO_2$ solution absorption and resonance Raman (Figure S1), $L10CuO_2$ mull absorption (Figure S2), $L3CuO_2$ IR spectra (Figure S3), $L1Cu^{II}(OH)_2$-$Cu^{II}L1$ mull absorption (Figure S4), additional MO energy level diagrams and contour surface plots (Figures S5−S7), normal coordinate analysis results (Table S1), additional MO energies and compositions (Tables S2 and S3), and molecular coordinates (Table S4) (PDF). This material is available free of charge via the Internet at http://pubs.acs.org.

JA020969I